Plasmon-enabled degradation of organic micropollutants in water by visible-light illumination of Janus gold nanorods

Haoran Wei[a,b], Stephanie K. Loeb[a,b], Naomi J. Halas[b,c,1], and Jae-Hong Kim[a,b,1]

[a]Department of Chemical and Environmental Engineering, Yale University, New Haven, CT 06511; [b]Nanosystems Engineering Research Center for Nanotechnology-Enabled Water Treatment, Rice University, Houston, TX 77005; and [c]Department of Chemistry, Rice University, Houston, TX 77005

The development of sustainable methods for the degradation of pollutants in water is an ongoing critical challenge. Anthropogenic organic micropollutants such as pharmaceuticals, present in our water supplies in trace quantities, are currently not remediated by conventional treatment processes. Here, we report an initial demonstration of the oxidative degradation of organic micropollutants using specially designed nanoparticles and visible-wavelength sunlight. Gold "Janus" nanorods (Au JNRs), partially coated with silica to enhance their colloidal stability in aqueous solutions while also maintaining a partially uncoated Au surface to facilitate photocatalysis, were synthesized. Au JNRs were dispersed in an aqueous solution containing peroxydisulfate (PDS), where oxidative degradation of both simulant and actual organic micropollutants was observed. Photothermal heating, light-induced hot electron-driven charge transfer, and direct electron shuttling under dark conditions all contribute to the observed oxidation chemistry. This work not only provides an ideal platform for studying plasmonic photochemistry in aqueous medium but also opens the door for nanoengineered, solar-based methods to remediate recalcitrant micropollutants in water supplies.

organic micropollutant | solar water treatment | plasmon resonance | persulfate-based advanced oxidation process

The optical excitation of noble or coinage nanoparticles at energies corresponding to their localized surface plasmon resonance (LSPR) induces the coherent oscillation of electrons (1). This strong light–matter interaction has been exploited for a wide range of applications, including bioimaging, sensing, and photocatalysis (2–4). In addition to large local electromagnetic field enhancements, LSPR excitation also gives rise to strong light-to-heat conversion (5, 6). Following the absorption of photons by the nanoparticle, the excited surface plasmons can decay into hot electron/hole pairs via Landau damping; the pairs thermalize to form a hot Fermi-Dirac–like distribution via electron–electron scattering, then equilibrate with the nanoparticle lattice through electron–phonon interactions (7). This photo-induced generation of heat results in an elevated temperature at the nanoparticle surface (7, 8). This localized heating effect has been employed to develop novel photothermal therapies; for example, the conversion of near-infrared radiation into heat for the highly localized induction of coagulative necrosis in cancerous tumors (9). The first successful clinical trial for photothermal ablation of human prostate tumor using gold nanoshells was recently reported (10).

Nanoparticle-based localized photothermal heating has recently attracted extensive attention as an innovative approach to harvest solar energy for water desalination and disinfection (11, 12). Upon solar illumination, dispersed collections of nanoparticles can efficiently convert water into steam by their intense optical absorption that, combined with multiple scattering events, concentrates light within a small spatial domain (8, 13, 14). Compared to conventional bulk heating, the steam production enabled by localized heating requires much less energy input, since the entire volume of water does not need to be heated. Accordingly, low-cost water

desalination technologies such as solar photothermal membrane distillation and solar distillation with zero liquid discharge have recently been demonstrated (11, 15–17). Photothermal nanomaterials have also been employed to produce potable water by capturing atmospheric water under dark conditions and releasing it using sunlight (18). Photothermally produced steam has been harnessed for other applications, such as medical instrument sterilization (8) or the off-grid production of cellulosic bioethanol (19). More recently, broadband absorbing photothermal nanoparticles were employed to inactivate waterborne pathogens under solar irradiation to develop low-cost water disinfection technologies (12, 20). To date, however, the majority of environmental applications remain based primarily on sunlight-induced liquid-to-vapor phase change.

Plasmonic photocatalysis by hot carriers (e^-/h^+ pair) is another important property of plasmonic nanoparticles (7). Since the first successful demonstration of the photoinduced reduction of Ag^+ to grow Ag nanocrystals by plasmonic hot electron transfer (21, 22), hot carrier-mediated reactions including hydrogen dissociation (23–25), ethylene epoxidation (26), CO oxidation (26), and NH_3 oxidation (26) have been reported. Efficient hot electron transport across the Schottky barrier in plasmonic nanoparticle/semiconductor heterojunctions has been instrumental for the development of plasmon-based optoelectronic devices (27, 28).

Significance

The presence of organic micropollutants, resulting from pesticide, solvent, detergent, or pharmaceutical use, in drinking water sources poses a significant threat to human health. Degrading these dangerous pollutants using advanced oxidation processes is a desirable but highly energy-intensive treatment option. Here, we report the solar oxidation of organic micropollutants, facilitated by nanorod particles specially designed both for photocatalytic reactivity and for stability under actively transforming water conditions induced by the photocatalytic process itself. Gold Janus nanorods, designed to harvest visible and near-infrared light, are demonstrated to cooperatively activate persulfate ions to generate free radicals for the oxidative decomposition of recalcitrant pollutants. This material platform presents an alternative approach to utilize sunlight for low-cost water purification.

ENGINEERING

Antenna–reactor complexes are an emerging class of plasmonic photocatalysts that combine the light-harvesting property of plasmonic nanoparticles (optical nanoantennas) with the catalytic reactivity of transition metal nanoparticles (reactors) (29–31). Zhou et al. (3) recently developed a theoretical framework for plasmonic photochemistry, quantifying the thermal and hot carrier contributions in ammonia decomposition by defining a light-induced lowering of the reaction barrier by the illuminated plasmonic photocatalyst. Despite growing interest, the possibility of using plasmonic photocatalysts for facilitating water pollution remediation chemistry has not yet been explored.

As an unfortunate by-product of global population and economic growth, many anthropogenic chemicals, such as pesticides, pharmaceuticals, and flame retardants, are being manufactured and unavoidably discharged into nature. These chemicals, often referred to as organic micropollutants due to their typically trace concentrations, are frequently found not only in natural water bodies such as river and lake but also in tap water, because they are not effectively remediated by conventional drinking water and wastewater treatment processes (32). Peroxydisulfate (PDS) $[E_0(S_2O_8^{2-}/2SO_4^{2-}) = +2.0$ V vs. standard hydrogen electrode (SHE)] is a promising alternative oxidant for water treatment (33, 34). In persulfate-based advanced oxidation processes (AOPs), PDS is activated by either the one-electron reduction of PDS or the homolytic cleavage of its O–O bond for the in situ production of highly reactive sulfate radicals $[E_0(SO_4^-\bullet/SO_4^{2-}) = +2.43$ V vs. SHE] (33). This activation process requires energy, in the form of light, sonication, and/or heat (35–37), or the addition of redox reagents such as transition metals (38, 39). Activating PDS using solar irradiation would be ideal, since sunlight is free, abundant, and easily accessible. However, PDS does not absorb light at wavelengths longer than 350 nm (40), making visible wavelength sunlight-induced PDS photolysis impossible.

Here, we investigate the use of plasmonic nanoparticles and visible-wavelength sunlight to degrade organic micropollutants in water. Common designs for plasmonic nanostructures, i.e., core–shell and simple surface loading (or deposition), often suffer from inefficient electron/hole separation/utilization, low photothermal conversion efficiency, poor colloidal stability, and high synthesis cost. We designed and synthesized "Janus" (41) Au nanorods (Au JNRs) partially coated with silica that can overcome these disadvantages. This partial silica coating provides stability in ionic solutions where uncoated nanorods would characteristically flocculate, while the exposed portion of the Au surface provides an active plasmonic surface for oxidative degradation chemistry. The presence or absence of hexadecyltrimethylammonium bromide (CTAB) coating on the exposed section of the nanorod, and its role in the chemical degradation process, is also studied. Fully silica-coated Au nanospheres (Au NSs/SiO₂) were also studied as a control. We hypothesize that photothermal heating by solar illumination of the Au JNRs can drive the homolytic cleavage of the PDS peroxide bond and produce sulfate radicals for organic pollutant degradation. We also examine how Au nanoparticles (Au NPs) with different morphologies degrade select pollutants, including emerging contaminants such as perfluorooctanoic acid (PFOA), with varying kinetics and through different mechanisms such as PDS activation through bulk heating, localized heating, and direct and light-induced electron transfer. This study represents an investigation of the use of plasmonic nanoparticles to drive an AOP directly relevant for water treatment, also providing an important use for nanophotonics in environmental remediation applications.

Results and Discussion

Improved Stability of Silica-Encapsulated Au NPs.
As-prepared Au NR [length = 54 ± 3 nm, diameter = 12 ± 1 nm, number of measurements (n) = 20, as previously reported (12, 42)] and Au NS [diameter = 13 ± 2 nm, n = 135, based on transmission electron microscopy (TEM) image analysis] were coated by CTAB and citrate ligands, respectively (*SI Appendix*, Figs. S1 and S2). While these ligands typically ensure colloidal stability in water, the addition of electrolyte, e.g., PDS, to these nanoparticle suspensions resulted in irreversible aggregation. Taking Au NRs as an example, we characterized their aqueous stability by monitoring the variation of longitudinal LSPR band intensity as a function of time (Fig. 1*A*). The band intensity decreased by 73% immediately after the addition of 86 mM NaCl and gradually declined to zero in 5 h. The loss of the LSPR peak was the result of Au NR aggregation and flocculation.

To overcome this limitation, we synthesized Au JNRs partially encapsulated with silica by employing a modified Stöber process (*SI Appendix*, Fig. S3). As previously reported (43, 44), the CTAB double layer binds strongly onto the (110) facet of Au NRs and cannot be easily displaced. By adding polyvinylpyrrolidone (PVP) at a high concentration, we partially displaced the CTAB layer on other facets of the Au NR surface with PVP and stabilized them in an ethanol/water cosolvent (note that the Stöber reaction proceeds only when ethanol is added; *SI Appendix*, Fig. S3) (45). As tetraethyl orthosilicate (TEOS) hydrolyzed, the newly formed SiO₂ preferentially deposited onto the PVP-functionalized Au NR surfaces to result in a partially encapsulated JNR. The asymmetric structure of the Au JNRs was confirmed by high-angle annular dark-field scanning TEM (HAADF-STEM) images, energy-dispersive X-ray spectroscopy (EDS) mapping, and scanning electron microscopy (SEM) images (Fig. 1*B* and *SI Appendix*, Figs. S4 and S5). Due to the presence of excess PVP in solution, SiO₂ NPs were also formed during this synthesis (*SI Appendix*, Fig. S5), which are chemically inert and do not affect the photochemistry investigated in this study.

Au NS/SiO₂ were synthesized using a similar method, as schematically illustrated in *SI Appendix*, Fig. S6. The fully encapsulated structure of Au NS/SiO₂ was confirmed by HAADF images and EDS mapping (Fig. 1*C* and *SI Appendix*, Fig. S7). SEM images at lower magnifications suggested no uncoated Au NSs and hollow SiO₂ NPs were present (*SI Appendix*, Fig. S8). The diameter of the core Au NS (12.9 ± 1.7 nm, n = 40) remained unchanged following SiO₂ coating, and the thickness of the added SiO₂ shell was determined to be 44.4 ± 8.0 nm (n = 70). This thick silica shell is expected to prevent contact between the Au NS and the reactants in water (i.e., PDS and pollutants).

Silica encapsulation significantly improved the colloidal stability of both types of Au NPs (*SI Appendix*, Figs. S9–S11). After silica coating, the longitudinal band intensity of Au JNRs remained constant over 5 h (Fig. 1*A*), indicating that agglomeration did not occur. Au JNR suspensions retained their strong optical absorption in the presence of 100 mM PDS for 24 h while the Au NRs severely agglomerated in the presence of 10 mM PDS (*SI Appendix*, Fig. S10). Similar improvements in colloidal stability were observed for Au NS/SiO₂ (*SI Appendix*, Fig. S11 *A*–*C*). The improved stability also enabled repeated washing and recovery of the Au NPs by centrifugation and resuspension (*SI Appendix*, Fig. S11*D*). Note that the Au NPs with improved colloidal stability reported in the past literature typically exhibit a core–shell structure (i.e., Au NP surface fully encapsulated by SiO₂) similar to our Au NS/SiO₂ (46–49). In contrast, the asymmetric Au JNRs are unique, exhibiting excellent stability in ionic solutions and also providing exposed Au surfaces available for chemical processes, such as plasmonic photocatalysis discussed below.

Optical and Photothermal Properties of Au NP/SiO₂. Both Au JNRs and Au NSs retained their plasmon resonance property after partial or complete silica encapsulation, respectively (Fig. 1*D*). Following silica encapsulation, the LSPR band of Au NSs was still distinguishable despite the spectrum exhibiting predominant
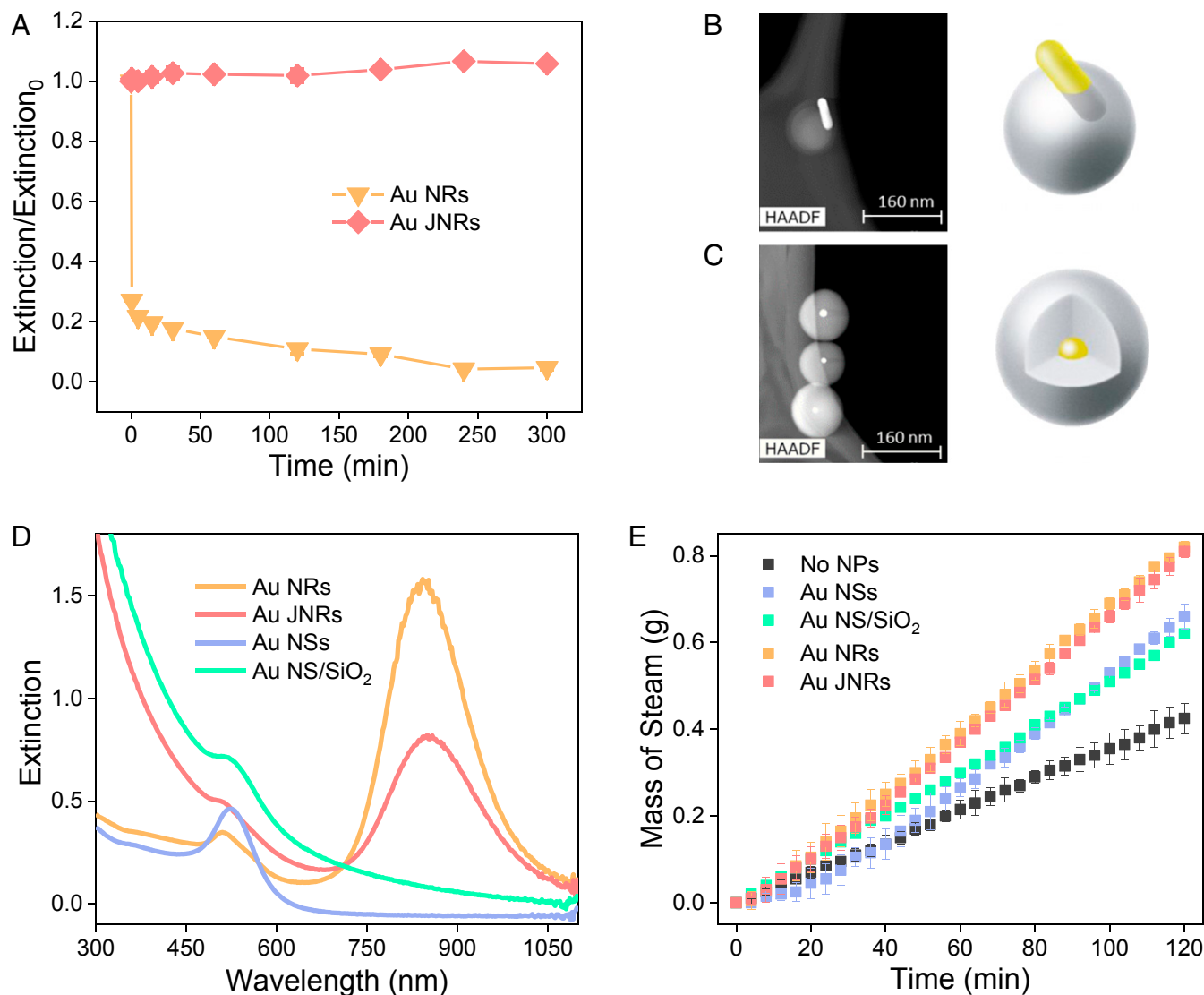
www.manaraa.com

Fig. 1. (*A*) Variation of the longitudinal LSPR band intensity of Au NRs and Au JNRs in the presence of 86 mM NaCl as a function of time. HAADF images and schematics of (*B*) Au JNR and (*C*) Au NS/SiO$_2$. (*D*) UV-VIS spectra of Au NR, Au JNR, Au NS, and Au NS/SiO$_2$ suspensions. (*E*) Accumulated mass of solar steam generated from aqueous suspensions of Au NRs, Au JNRs, Au NSs, and Au NS/SiO$_2$.

features of the SiO$_2$ scattering spectrum. Since SiO$_2$ NP scatters UV light, but not visible or infrared light (50), a significant portion of sunlight would penetrate the shell and reach the Au NS core. Au NRs exhibited a transverse LSPR band at 508 nm and a longitudinal LSPR band at 842 nm. Following silica encapsulation, the longitudinal band red-shifted to 858 nm due to the increase in the dielectric constant of the surrounding medium (ε_m) (51). This increase in ε_m results in a decrease of the real part of the dielectric function of gold (ε_1) when the condition of maximum extinction (i.e., sum of absorption and scattering) is met ($\varepsilon_1 = -2\varepsilon_m$) (1). This in turn leads to an increase in the maximum extinction wavelength due to its negative correlation with ε_1. The decrease of the primary LSPR band intensities for Au NRs (858 nm) and Au NSs (522 nm) following silica encapsulation is likely due to a loss of Au NPs during the washing process.

The rate of solar steam generation by the Au JNR and Au NS suspensions was 42 to 62% faster than the rate of pure water without nanoparticles, confirming that the nanoparticle-induced localized photothermal heating is sufficient for vaporizing water,

i.e., the surface temperature of Au NPs is substantially higher than that of the bulk suspension (Fig. 1*E*). The slower rate of Au NSs during the initial 40 min is possibly due to the oxidation of citrate by the hot holes (52). The hot carrier-mediated reaction is an alternative channel for LSPR relaxation (7), thus allowing less energy to be converted into heat. This hypothesis was supported by the aggregation of Au NSs under simulated sunlight illumination, which indicated that the stabilizing citrate layer was most likely to be compromised (*SI Appendix*, Fig. S12). Although the photothermal effect of plasmonic nanoparticles has been well documented (8, 13), the influence of silica encapsulation has not been reported. The rates of steam generation by Au NRs and Au JNRs were very similar (Fig. 1*E* and *SI Appendix*, Table S1), indicating that partial silica coating did not affect steam generation. However, the rate of steam generation by Au NS/SiO$_2$ was 24% lower than that by Au NSs (Fig. 1*E* and *SI Appendix*, Table S1), indicating that the ability of Au NSs to produce steam was affected after they were fully coated with a thick silica shell. This was further supported by the lower equilibrated temperature of bulk Au NS/SiO$_2$ suspensions compared to that of Au NS

Wei et al.

ENGINEERING

www.manaraa.com

suspensions (*SI Appendix*, Fig. S13). The kinetics of steam generation followed a zeroth-order model, and the rate constants are listed in *SI Appendix*, Table S1.

Solar Photothermal Degradation of Organic Pollutants: The Role of Bulk Water Heating. The photothermal response of Au NPs was observed by monitoring the increase in the bulk water temperature under solar simulator illumination (Fig. 2*A*). We first examined whether photothermal heating was sufficient to drive PDS-mediated degradation of a model micropollutant, phenol, by measuring its degradation kinetics in the presence of PDS and Au NPs (or Au NP/SiO$_2$) (Fig. 2*B*). No phenol degradation was observed in the presence of PDS for 2 h under dark conditions, while under sunlit conditions, phenol was slowly decomposed by PDS following pseudo–first-order kinetics ($k = 2.2 \times 10^{-3}$ min^{-1}; *SI Appendix*, Table S2). The degradation was due to the increase of bulk water temperature from 22 to 37 °C (Fig. 2 *A* and *B*). This increase in water temperature is likely due to the absorption of infrared light. The rate constant for phenol degradation increased by 18% in the presence of Au NS/SiO$_2$ (*SI Appendix*, Table S2), while the bulk water temperature increased from 37 to 43 °C (Fig. 2 *A* and *B*). This moderate increase in phenol

Fig. 2. (*A*) Increase in bulk temperature of suspensions containing Au NS/SiO$_2$, Au NRs, and Au JNRs. (*B*) Degradation kinetics of phenol in PDS solutions containing Au NS/SiO$_2$, Au NRs, and Au JNRs ([PDS]$_0$ = 10 mM; [phenol]$_0$ = 100 μM; temperature, 22 °C under dark conditions; illumination, 4 Sun).

degradation rate indicates that bulk temperature alone does play a relatively minor role in PDS-mediated phenol degradation.

Au NRs degraded phenol significantly faster ($k = 7.1 \times 10^{-3}$ min^{-1}) than Au NS/SiO$_2$. CTAB is known to react with PDS (53), which may generate SO$_4^-$• for phenol oxidation. This possibility was eliminated, since no phenol degradation by Au NRs was observed under dark conditions (*SI Appendix*, Fig. S14). Au NRs heated the bulk water to 48 °C, which might account for its faster phenol degradation than Au NS/SiO$_2$ (Fig. 2*A*). However, Au JNRs heated the bulk water to the same temperature, but exhibited a phenol degradation rate 21 times higher ($k = 0.15$ min^{-1}). This clearly indicates that mechanisms other than bulk water heating are important in the Au JNR-mediated photocatalysis of phenol degradation. Compared to CTAB-capped Au NRs, the Au JNRs were washed nine times, which is likely to remove much of the CTAB from the Au NR surface (*SI Appendix*, Fig. S3). This expectation is consistent with the fact that phenol degradation was much slower in the presence of unwashed Au JNRs (*SI Appendix*, Fig. S15). A negligible amount of phenol would transfer to the headspace of the quartz cuvette (molar ratio between phenol in gaseous and aqueous phases: $n_{gas}/n_{aqueous} = 3 \times 10^{-6}$; Henry's law constant = 1,270 mol kg^{-1}·bar^{-1} at 48 °C; aqueous solution volume, 4.5 mL; headspace volume, 0.5 mL). Therefore, we hypothesize that the rapid increase in phenol degradation is related to the exposed Au JNR surface. The Au JNR nanostructures remained stable after the photocatalytic process as supported by visual observations and the control experiments (*SI Appendix*, Fig. S16). Since the Au JNRs exhibited the fastest phenol degradation kinetics, it was employed for the experiments described below.

Role of the Au NR/Water Interface. To further elucidate the mechanism of phenol degradation in the presence of Au JNRs and light, we studied the degradation kinetics under dark conditions in the environmentally relevant pH range of 5 to 9 (Fig. 3*A*). Phenol was readily degraded under dark conditions with a rate constant of $0.95–1.5 \times 10^{-2}$ min^{-1}. Recently, it has been reported that noble metals (e.g., Pd, Pt, Au, Rh, Ir) in nanoparticulate form can activate peroxymonosulfate (PMS) and degrade phenol without generating free radicals (54, 55). Noble metals are thus considered to be "electron shuttles" between PMS (electron acceptor) and organic pollutants (electron donor). If the exposed Au surfaces were involved in phenol degradation, direct electron transfer from the phenol to PDS would occur without illumination. To further confirm the direct electron transfer, methanol was added as the SO$_4^-$• and OH• quencher (their second-order rate constants are both on the order of 10^{-9} M^{-1}·s^{-1}) (56). Under dark conditions, the kinetics of phenol degradation did not change following the addition of methanol, indicating that phenol was being degraded through a nonradical process (Fig. 3*B*). These results collectively support the hypothesis that phenol can directly transfer its electrons to PDS via Au JNRs, which serve as an electron transfer mediator.

Interestingly, under sunlit conditions, the rate constants for phenol degradation increased by 3 to 10 times (Fig. 3*A*), suggesting that localized photothermal heating also plays a critical role in the degradation process. Heat can break the O–O bond of PDS and produce two SO$_4^{•-}$ (33, 36). It is possible that sulfate radicals were produced during phenol degradation under sunlit conditions. The addition of methanol significantly inhibited phenol degradation under simulated solar illumination, confirming free radical production (Fig. 3*B*). When no electron donor was added, PDS did not react in the nanoparticle suspension under dark conditions, but decomposed under solar illumination (*SI Appendix*, Fig. S17). This observation further supports our speculation. The addition of 50 mM HCO$_3^-$ (an anion commonly present in surface water) had a negligible effect on the phenol degradation rate under both dark and sunlit conditions (*SI Appendix*, Fig. S18) because HCO$_3^-$ exhibits a
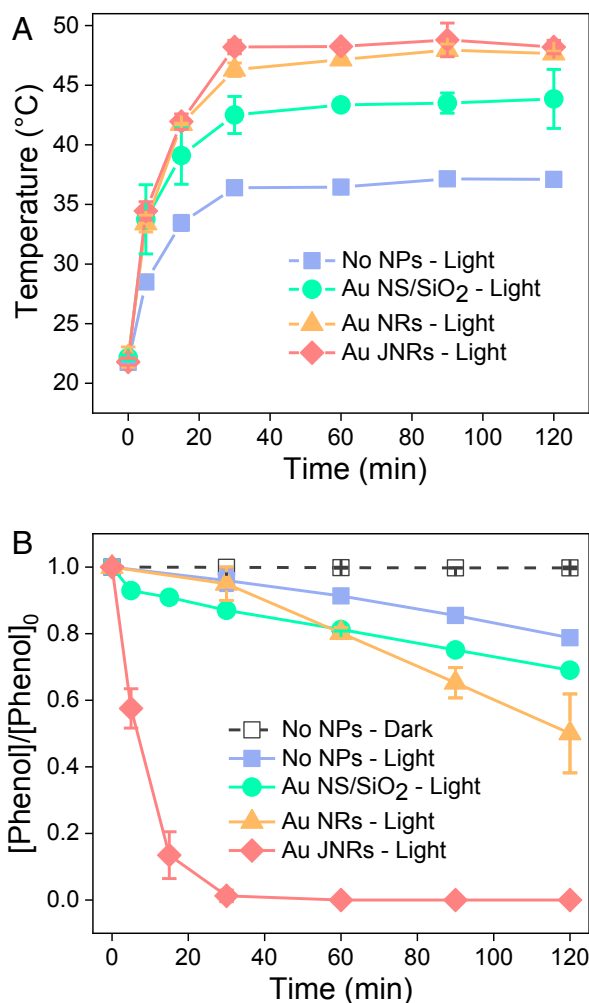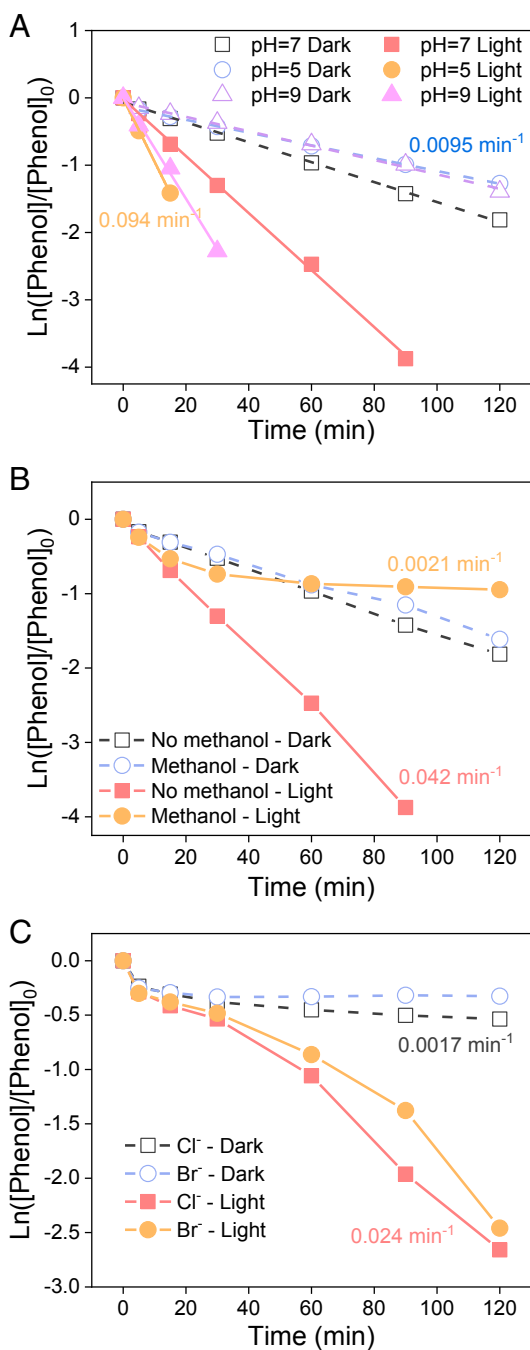
www.manaraa.com

Fig. 3. (A) Degradation kinetics of phenol under both dark and sunlit conditions in water environments with different pH ([PDS]$_0$ = 10 mM, [phenol]$_0$ = 100 μM, [phosphate buffer (PB)] = 10 mM; pH 5 to 9; temperature, 22 °C under dark conditions). (B) Influence of free radical quencher – methanol on the degradation kinetics of phenol under both dark and sunlit conditions ([PDS]$_0$ = 10 mM, [phenol]$_0$ = 100 μM, [PB] = 10 mM, [methanol]$_0$ = 200 mM; pH 7; temperature, 22 °C under dark conditions). (C) Influence of Cl$^-$ and Br$^-$ on the degradation kinetics of phenol under both dark and sunlit conditions ([PDS]$_0$ = 10 mM, [phenol]$_0$ = 100 μM, [PB] = 10 mM, [Cl$^-$]$_0$ = [Br$^-$]$_0$ = 50 mM; pH 7; temperature, 22 °C under dark conditions). Au JNRs were used in these experiments.

poor affinity for Au NR surfaces, like most anions in natural water systems.

When 50 mM Cl$^-$ was added to the solution, phenol degradation was significantly inhibited under dark conditions (Fig. 3C

and *SI Appendix*, Table S2). Some anions, such as the halides, exhibit a high affinity for Au NP surfaces, poisoning the surface and greatly arresting photocatalytic degradation. Chloride ions can form a covalent Au–Cl bond with an Au surface (57). Therefore, the Cl$^-$ covered Au NR surfaces may severely limit direct electron transfer from phenol to PDS, leading to an inhibition of phenol degradation under dark conditions. Significantly different behaviors of Cl$^-$ and HCO$_3^-$ in inhibiting the direct electron transfer under dark conditions indicate that the electrostatic attraction is not the main reason for this inhibition. However, under illumination, the phenol degradation rate increased 14 times (Fig. 3C), indicating that the solar-illuminated Au JNRs efficiently removed phenol in the presence of 50 mM Cl$^-$. Similar results were observed when 50 mM Br$^-$ was added (Fig. 3C). In the presence of Br$^-$, phenol degradation was completely inhibited under dark conditions, while it readily proceeded under sunlit conditions. This can be attributed to the generation of SO$_4^-$• under sunlit conditions that directly oxidized the phenol in solution. To further quantify the contribution of the radical process, phenol removal under dark conditions was subtracted from that under illumination, before and after the addition of Cl$^-$ (*SI Appendix*, Fig. S19). The rate of phenol degradation contributed solely from the radicals decreased by 51% following Cl$^-$ addition. It has been reported that Cl$^-$/Br$^-$ deteriorated the performance of UV/persulfate-AOP because SO$_4^-$• can oxidize Cl$^-$/Br$^-$ and generate less reactive species (e.g., Cl• and Br•) (58, 59).

The Role of Localized Heating. As shown in Fig. 4A, bulk heating (i.e., heating the water to 48 °C; Fig. 2A) resulted in a phenol degradation rate constant of 0.0071 min^{-1}, while the electron shuttle effect led to a rate constant of 0.015 min^{-1}. The sum of these two numbers (0.022 min^{-1}) was only 52% of the overall phenol degradation rate constant obtained under sunlit conditions (Fig. 4A). Consequently, the contribution from combined bulk heating and electron shuttle effects still cannot fully explain the fast phenol removal rate observed in this study. The LSPR of Au NRs elicits unique localized effects within nanoscale proximity of their surfaces, including the higher temperature than bulk solution (localized heating) and light-induced charge separation (hot electron generation). Since the bulk suspension temperature in this study (48 °C) is close to that usually adopted for thermal PDS activation (50 °C) (60, 61), the localized temperature on Au JNR surface should be sufficient for generating sulfate radicals from PDS. To explain our observations more comprehensively, we examine the possibility that localized heating due to plasmon excitation and hot electron generation may also contribute to the degradation rate (8, 13). We propose mechanisms for solar phenol degradation using the schematic shown in Fig. 4 B and C. Under dark conditions, phenol transfers its electrons to PDS (mechanism 1: electron shuttle effect; Fig. 4B), which accounts for 35% of the overall phenol degradation rate. Upon simulated solar illumination, photothermal heating effect by the Au JNRs results in an increase of bulk water temperature to 48 °C (mechanism 2: bulk heating effect; Fig. 4C), accounting for 17% of overall phenol degradation rate. Higher local temperatures and plasmonic hot electron transfer (mechanism 3: localized effects; Fig. 4C) account for 48% of the overall phenol degradation rate.

Some compounds such as benzoic acid cannot directly transfer electrons to PDS due to their high redox potential (56). As shown in Fig. 4D, the concentration of benzoic acid remained constant in 2 h under dark conditions, showing that mechanism 1 contributed negligibly to the overall benzoic acid degradation rate. However, under illumination conditions, it was readily degraded by the photothermally produced sulfate radicals. By heating the bulk solution to 48 °C under dark conditions, the degradation rate of benzoic acid contributed by mechanism 2 was
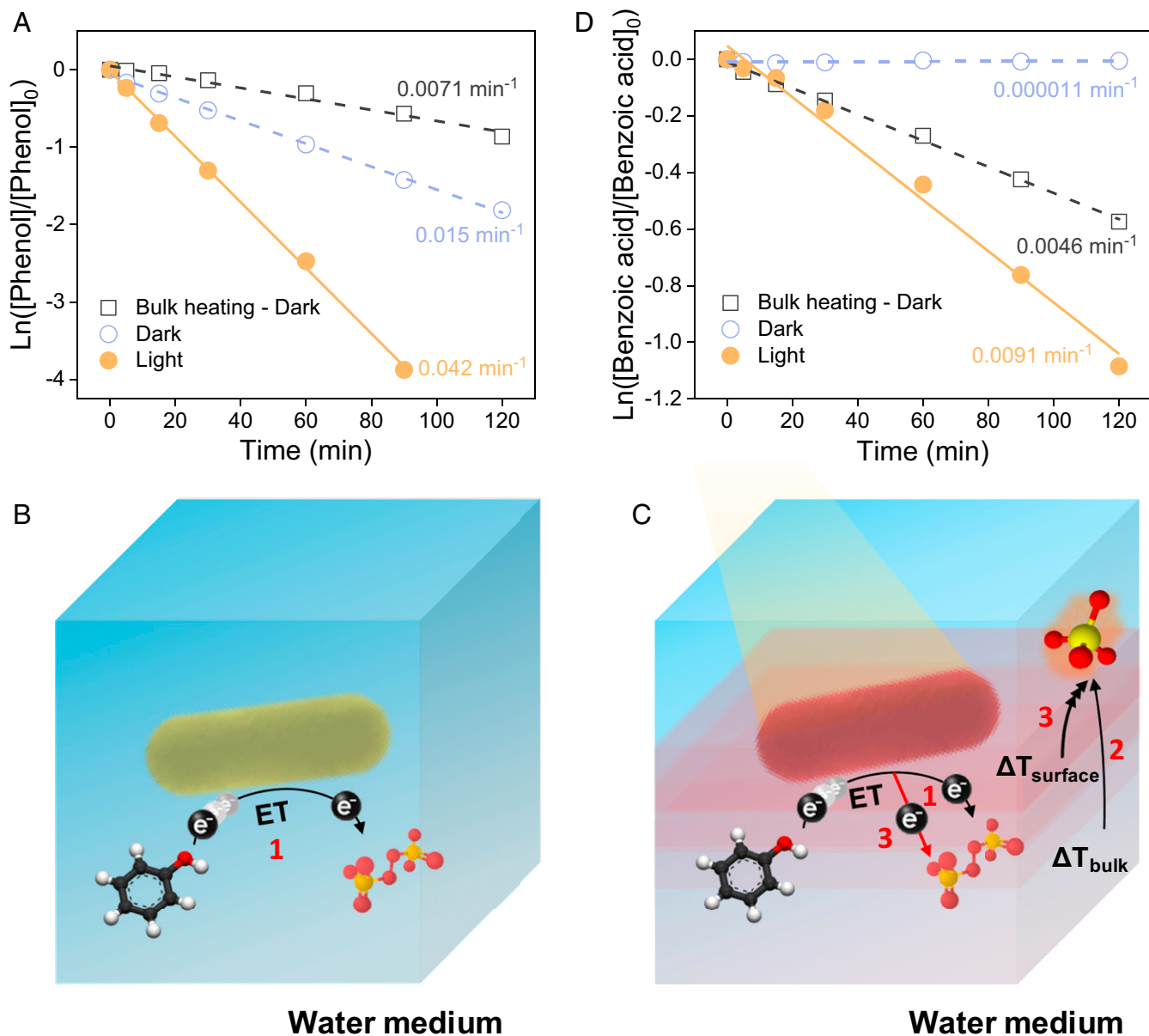
Fig. 4. (*A*) Degradation kinetics of phenol acquired by heating the bulk solution to the equilibrium temperature obtained under simulated sunlight illumination ($[PDS]_0 = 10$ mM, $[phenol]_0 = 100$ μM, $[PB] = 10$ mM; pH 7; temperature, 22 or 48 °C under dark). Schematic of the mechanisms involved in phenol degradation under (*B*) dark and (*C*) sunlit conditions. ET, electron transfer; ΔT_{bulk}, temperature increase in bulk solution; $\Delta T_{surface}$, temperature increase at nanorod surface. (*D*) Degradation kinetics of benzoic acid under either dark or light conditions ($[PDS]_0 = 10$ mM, $[benzoic\ acid]_0 = 100$ μM, $[PB] = 10$ mM; pH 7; temperature, 22 or 48 °C under dark). Au JNRs were used in all these experiments.

obtained, which accounted for 51% of the overall benzoic acid degradation rate. The bulk solutions with and without Au JNRs exhibited similar kinetics for benzoic acid degradation upon bulk heating (*SI Appendix*, Fig. S20). Therefore, mechanism 3, the localized effect, contributed 49% of the overall benzoic acid degradation rate, which is consistent with the results obtained with phenol. The rates of plasmonic photocatalytic reactions and the solar photothermal desalination both follow a superlinear power law dependence on light intensity (17, 62). The overall dependence of pollutant degradation efficiency on light intensity in our system is a result of collective contributions from multiple mechanisms, which is challenging to deconvolute experimentally. This study is focused on plasmon-enabled interfacial photoreactions (Fig. 4 *B* and *C*). The subsequent solution-based reactions between sulfate radicals and organic chemicals, including

kinetics, mechanisms, and pathways, have been documented in detail in our recent review paper (63).

Plasmonic hot electron-mediated photocatalysis is a rapidly developing field due to its unique advantages over conventional photocatalysis, such as reduced activation barrier and high selectivity to specific reaction products (3, 64). It has been reported that the plasmonic hot electrons can transfer into the conduction band of semiconductors via injection across the Schottky barrier (indirect plasmon-induced charge transfer) or via chemical interface damping mechanism (direct plasmon-induced charge transfer) (64). Hot electrons can also induce the dissociation of an H_2 molecule by transferring into its Feshbach resonance (25) and facilitate O_2 dissociation by transferring into its antibonding orbital (26). In this study, our results suggest that the plasmonic hot electrons can activate peroxide bond and produce highly

www.manaraa.com

reactive free radicals. Hot holes in Au are excited at 2.6 to 2.8 eV, which is just above the interband transition in Au at 442 to 476 nm (65). However, Au JNRs absorbs photons primarily at 1.30 to 1.65 eV (750 to 950 nm; Fig. 1D), which has sufficient energy only for the generation of hot electrons, not hot holes. The strong Rayleigh scattering of silica on Au and in solution further inhibits the light absorption by Au JNRs at energies that are high enough for hot hole generation. In addition, most of current plasmonic photocatalytic platforms are prepared by expensive lithographic methods and are only used for driving reactions in gaseous phase. In contrast, the Au JNR platform is synthesized via a scalable bottom-up method and is demonstrated to drive aqueous reactions. These unique advantages over conventional (plasmonic) photocatalysis makes Au JNR plasmonic platform very promising for solar degradation of recalcitrant water pollutants.

Solar Degradation of Organic Micropollutants. We examined the degradation of select organic micropollutants such as bisphenol A (BPA), amoxicillin, and PFOA, using solar simulator-illuminated Au JNRs. BPA is an important raw material for making polycarbonate and epoxy resins. The occurrence of BPA in both surface and underground waters poses risks to human health due to endocrine disruption (66). BPA was rapidly degraded under dark conditions until reaching a plateau at ~50% removal (Fig. 5A). The near-complete inhibition of the "electron shuttle" effect in 30 min was similar to that in the presence of Cl^-, giving rise to the possibility that some BPA oxidation products may passivate the Au surface. It has been reported that polymeric substances can be generated during the oxidation of BPA by manganese oxide through radical coupling (67). These polymers may prevent the electron transfer between PDS and BPA. However, under sunlit conditions, BPA was rapidly degraded and reached a 100% removal rate in 30 min (Fig. 5A). Amoxicillin is a widely used antibiotic that poses emerging concern due to its frequent occurrence in surface waters (68). Under both dark and illumination conditions, a removal rate of ~15% was observed in 5 min due to its adsorption onto Au NR surface by forming Au–S covalent bonds (Fig. 5B). This low removal rate is attributed to the low adsorbent-to-adsorbate mass ratio. Afterward, only slight amoxicillin degradation was observed during 2 h under dark conditions, most likely because amoxicillin has a high redox potential that makes it challenging to transfer electrons to persulfate via Au JNRs. On the contrary, under sunlit conditions, amoxicillin was readily degraded and achieved a removal of 43% in 2 h. PFOA has attracted tremendous attention recently due to its biotoxicity and persistency in the environment (69). While PFOA concentration remained

constant for 3 h under dark conditions, it decreased by 13% under sunlit conditions (Fig. 5C). These results suggest that the solar photothermal effect of Au JNRs can be used to effectively degrade certain organic micropollutants with an efficiency that depends on the specific type of molecule.

This study reports visible-wavelength solar degradation of aqueous organic micropollutants using specially designed plasmonic nanoparticles. Partially coating Au NRs with silica to form Janus NRs creates a plasmonic nanoparticle with a high stability in a wide range of aqueous solutions as well as a reactive surface available to drive persulfate-based advanced oxidation. Several mechanisms appeared to have contributed to the degradation of a model pollutant, phenol, to environmentally benign products, such as hydrogen oxalate (*SI Appendix, Text S1* and Fig. S21), including electron shuttling under dark conditions and plasmonic effects such as bulk and localized heating and hot electron transfer. These combined processes were also demonstrated to degrade select micropollutants of current concern, including BPA, amoxicillin, and PFOA. This initial demonstration of the design and engineering of stabilized, solar plasmonic nanoparticles for micropollutant remediation opens the door to applications of plasmonics that address a critical environmental need. Due to its untapped fundamental advantages and low requirement on infrastructure investment, this technology is promising for a decentralized water treatment application in regions with abundant solar energy. In the future, recognition and quantitation of reactive species and intermediate products of plasmon-enabled pollutant degradation as a function of water chemistry, such as pH, ionic strength, and organic substrates, will be conducted in detail. Moving up technology readiness levels, issues regarding photoreactor scaling up and ways to reduce material cost will also be considered. This study employs the plasmonic photothermal and hot electron-mediated photocatalysis to drive an AOP in aqueous phase. Deconvolution of the contributions from each mechanism allows further optimization of this process in the future, including higher light-to-heat conversion and hot electron transfer efficiency. This work also bridges the plasmonic hot carrier-mediated photocatalysis and sulfate radical chemistry, which may have implications on light-controlled free radical-mediated reactions, such as free radical polymerization.

Methods

Materials. Gold chloride trihydrate ($HAuCl_4 \cdot 3H_2O$), PVP (average molecular weight, 40,000), potassium persulfate, L-ascorbic acid, CTAB, silver nitrate, benzoic acid, TEOS, phenol, BPA, PFOA, ammonium hydroxide (28 to 30% NH_3 basis), and sodium phosphate monobasic dihydrate were purchased from Sigma-Aldrich. Sodium citrate dihydrate ($Na_3Cit \cdot 2H_2O$) and methanol were acquired from J. T. Baker. Sodium borohydride ($NaBH_4$),

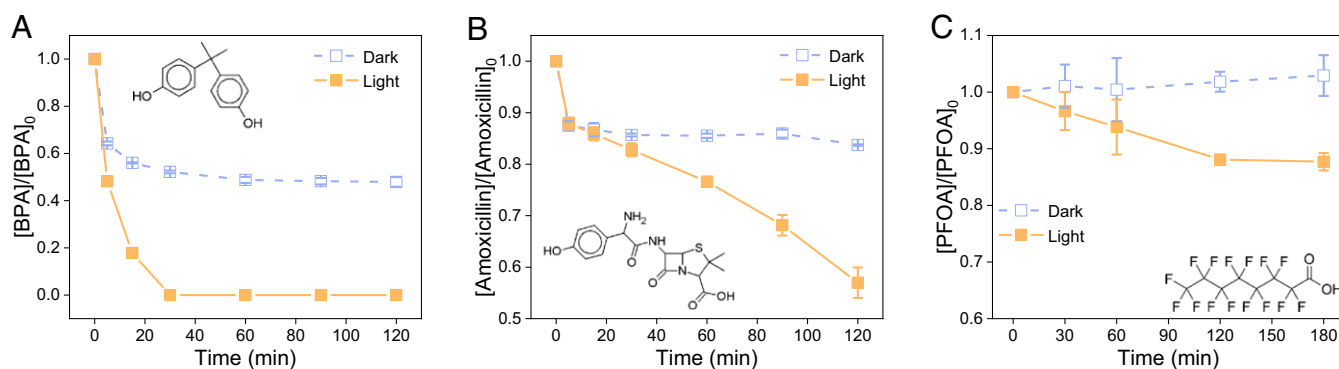**Fig. 5.** Degradation kinetics of (A) BPA, (B) amoxicillin, and (C) PFOA in Au JNR suspension under dark and sunlit conditions ($[PDS]_0 = 10$ mM, $[BPA]_0 = [amoxicillin]_0 = [PFOA]_0 = 100$ μM, $[PB] = 10$ mM; pH 7; temperature, 22 and 48 °C under dark and sunlit conditions). Au JNRs were used in all of these experiments.

Wei et al.

sodium phosphate dibasic, and ethanol were obtained from Fluka, Fisher Chemical, and Decon Labs, respectively.

Synthesis of Au JNRs. Au NRs were synthesized using a seed-mediated growth method (*SI Appendix*, *Text S2*) (12, 42). Briefly, Au NR seeds were prepared by adding 0.6 mL of $NaBH_4$ solution (10 mM) to a 10-mL mixture containing 0.25 mM $HAuCl_4$ and 97.5 mM CTAB. The mixture was left at room temperature for 2 h to allow for seed formation. The growth of Au NRs was initiated by adding 0.096 mL of the seed suspension into a mixture containing 0.46 mM $HAuCl_4$, 91.7 mM CTAB, 0.09 mM $AgNO_3$, 0.74 mM ascorbic acid, and 18 mM HCl. The high concentration of CTAB was selected to ensure the colloidal stability and anisotropic growth of Au NRs during the synthesis process. The mixture was kept under dark conditions overnight, and then washed twice by centrifugation and resuspended in water. The Au JNRs were synthesized using a modified Stöber approach (*SI Appendix*, Fig. S3). Briefly, an aliquot of 0.5 mL of PVP (0.88 M) was added into 25 mL of Au NR suspension (8.5×10^{12} particles/mL). Following vigorous vortexing, an aliquot of 5 mL of ethanol was added to the 2.5-mL PVP/Au NR suspension followed by the addition of 250 μL of ammonium hydroxide and 125 μL of TEOS. The mixture was shaken for 24 h to complete the growth of the silica shell. After synthesis, Au JNRs were washed extensively to remove CTAB and ethanol (which can act as a radical quencher) according to the following procedures. As-synthesized Au JNR suspension (5 mL) was diluted by 5× using ethanol. The diluted Au JNR suspension was then centrifuged and twice resuspended in ethanol. Following centrifugation, the pellet was resuspended in 10 mL of PDS solution (10 mM). The Au JNRs were then centrifuged and resuspended in 10 mL of PDS solution another six times, keeping the pellet collected after the last centrifugation for future use.

Synthesis of Core–Shell Au NS/SiO_2 Nanohybrids. Au NSs were synthesized using the citrate reduction method (see details in *SI Appendix, Text S3*). Briefly, an aliquot of 1.3 mL of Na_3Cit solution at a concentration of 150 mM was added into 48.7-mL boiling $HAuCl_4$ solution (1 mM) under vigorous stirring. The core–shell Au NS/SiO_2 nanohybrids were synthesized using a modified Stöber approach (*SI Appendix*, Fig. S6) (70). An aliquot of 0.18 mL of PVP at a concentration of 0.88 M was added to 25-mL Au NS suspension (4.5×10^{14} particles/mL). Following vigorous vortexing, 4 mL of ethanol was added to 2 mL of PVP-coated Au NS suspension, followed by the addition of 200 μL of ammonium hydroxide and 100 μL of TEOS. The mixture was shaken for 24 h to complete the growth of the silica shell. For the washing steps, an aliquot of 2-mL as-synthesized Au NS/SiO_2 suspension was diluted by 12.5× using ethanol, followed by ethanol removal as described above for Au JNRs.

Characterization. Nanoparticle morphologies were characterized by field emission SEM (Hitachi; SU8230) and TEM (FEI Tecnai Osiris). Samples for SEM and TEM imaging were prepared by drop casting a 5-μL nanoparticle suspension onto a silica wafer and a copper grid, respectively. SEM images were acquired using a secondary electron detector at 10 kV. Elemental mapping of silica and gold was achieved using HAADF-STEM coupled with EDS. Optical properties of the Au NPs were characterized using UV-VIS spectrophotometer (Agilent Cary 50). Simulated sunlight was generated by a solar simulator (ABET) with an illumination intensity at ~400 mW/cm^2 (4 Sun). To avoid PDS photolysis, the UV portion of the light was removed using a

400-nm long-pass filter. Concentrations of phenol, BPA, benzoic acid, amoxicillin, PFOA, and PDS were analyzed using high-performance liquid chromatography (HPLC) (Agilent 1100) equipped with a UV detector (see details in *SI Appendix*, Table S3). The phenol degradation products were analyzed using the electrospray ionization–mass spectrometer (Waters; LC/MS ZQ 4000) with the negative ion mode.

Solar Photothermal Response. The solar photothermal response of Au NRs, Au NSs, Au JNRs, and Au NS/SiO_2 was characterized by measuring the variation of bulk water temperature as a function of irradiation time with simulated sunlight (4 Sun, UV blocked). An aliquot of 4.5 mL of the nanoparticle suspension was added to a closed quartz cell, which was placed under the solar simulator (*SI Appendix*, Fig. S22A). The photothermal response was also characterized by measuring the loss of water from the aqueous suspensions. A 4-mL aliquot of the suspension was added to a beaker, with the illumination directed from above (*SI Appendix*, Fig. S22B). The mass concentrations of gold in different suspensions were kept constant.

Solar Photothermal Degradation of Organic Micropollutants. A 4-mL aliquot of PDS solution (10 mM) was added to a 15-mL centrifuge tube containing a pellet of nanoparticles. The nanoparticles were resuspended in the PDS solution following manual shaking for several seconds and remained as a stable colloid throughout the reaction period. A 0.4-mL aliquot of phenol (1 mM) was added to initiate the redox reaction. A mixture of PDS and phenol without Au NPs was used as a control. These mixtures were prepared in parallel with one kept under dark condition and the other one placed under simulated sunlight. A 0.25-mL aliquot of the suspension was withdrawn from the mixture at 5, 15, 30, 60, 90, and 120 min. Following centrifugation, a 0.1-mL aliquot of supernatant was withdrawn for HPLC analysis. Experiments were repeated at least in duplicate.

To investigate the influence of solution pH on pollutant degradation, a 90-μL aliquot of phosphate buffer (PB) (0.5 M) over a range of environmentally relevant pH values (5–9) was added to the suspension, followed by the addition of 0.4 mL of phenol (1 mM). To investigate the influence of halide ions on PDS activation, a 200-μL NaCl or NaBr solution (1 M) was added to the Au JNR suspension containing 10 mM PDS and 10 mM PB, followed by the addition of 0.4 mL of phenol (1 mM). To investigate the influence of bicarbonate on PDS activation, a 200-μL $NaHCO_3$ solution (1 M) was added to the Au JNR suspension containing 10 mM PDS between the addition of 90 μL PB (0.5 M, pH 7) and 0.4 mL phenol (1 mM). To investigate the influence of an electron donor on PDS activation, a 0.4-mL benzoic acid, BPA, amoxicillin, or PFOA solution with a concentration of 1 mM was added to a 4-mL Au JNR suspension containing 10 mM PDS and 10 mM PB (pH 7). The degradation kinetics of pollutants was obtained following the same procedure described above.

Data Availability Statement. All data necessary for replication are presented in the main text or *SI Appendix*.

1. K. M. Mayer, J. H. Hafner, Localized surface plasmon resonance sensors. *Chem. Rev.* **111**, 3828–3857 (2011).

2. N. Gandra, S. Singamaneni, Bilayered Raman-intense gold nanostructures with hidden tags (BRIGHTs) for high-resolution bioimaging. *Adv. Mater.* **25**, 1022–1027 (2013).

3. L. Zhou *et al.*, Quantifying hot carrier and thermal contributions in plasmonic photocatalysis. *Science* **362**, 69–72 (2018).

4. J. Pérez-Juste, I. Pastoriza-Santos, L. M. Liz-Marzán, P. Mulvaney, Gold nanorods: Synthesis, characterization and applications. *Coord. Chem. Rev.* **249**, 1870–1901 (2005).

5. D. J. De Aberasturi, A. B. Serrano-Montes, L. M. Liz-Marzán, Modern applications of plasmonic nanoparticles: From energy to health. *Adv. Opt. Mater.* **3**, 602–617 (2015).

6. P. K. Jain, X. Huang, I. H. El-Sayed, M. A. El-Sayed, Noble metals on the nanoscale: Optical and photothermal properties and some applications in imaging, sensing, biology, and medicine. *Acc. Chem. Res.* **41**, 1578–1586 (2008).

7. M. L. Brongersma, N. J. Halas, P. Nordlander, Plasmon-induced hot carrier science and technology. *Nat. Nanotechnol.* **10**, 25–34 (2015).

8. O. Neumann *et al.*, Solar vapor generation enabled by nanoparticles. *ACS Nano* **7**, 42–49 (2013).

9. L. R. Hirsch *et al.*, Nanoshell-mediated near-infrared thermal therapy of tumors under magnetic resonance guidance. *Proc. Natl. Acad. Sci. U.S.A.* **100**, 13549–13554 (2003).

10. A. R. Rastinehad *et al.*, Gold nanoshell-localized photothermal ablation of prostate tumors in a clinical pilot device study. *Proc. Natl. Acad. Sci. U.S.A.* **116**, 18590–18596 (2019).

11. L. Zhou *et al.*, 3D self-assembly of aluminium nanoparticles for plasmon-enhanced solar desalination. *Nat. Photonics* **10**, 393 (2016).

12. S. Loeb, C. Li, J. H. Kim, Solar photothermal disinfection using broadband-light absorbing gold nanoparticles and carbon black. *Environ. Sci. Technol.* **52**, 205–213 (2018).

13. N. J. Hogan *et al.*, Nanoparticles heat through light localization. *Nano Lett.* **14**, 4640–4645 (2014).

14. S. Baral, A. J. Green, M. Y. Livshits, A. O. Govorov, H. H. Richardson, Comparison of vapor formation of water at the solid/water interface to colloidal solutions using optically excited gold nanostructures. *ACS Nano* **8**, 1439–1448 (2014).

15. C. Finnerty, L. Zhang, D. L. Sedlak, K. L. Nelson, B. Mi, Synthetic graphene oxide leaf for solar desalination with zero liquid discharge. *Environ. Sci. Technol.* **51**, 11701–11709 (2017).

16. P. D. Dongare *et al.*, Nanophotonics-enabled solar membrane distillation for off-grid water purification. *Proc. Natl. Acad. Sci. U.S.A.* **114**, 6936–6941 (2017).

17. P. D. Dongare, A. Alabastri, O. Neumann, P. Nordlander, N. J. Halas, Solar thermal desalination as a nonlinear optical process. *Proc. Natl. Acad. Sci. U.S.A.* **116**, 13182–13187 (2019).

18. P. Wang, Emerging investigator series: The rise of nano-enabled photothermal materials for water evaporation and clean water production by sunlight. *Environ. Sci. Nano* **5**, 1078–1089 (2018).

19. O. Neumann *et al.*, Combining solar steam processing and solar distillation for fully off-grid production of cellulosic bioethanol. *ACS Energy Lett.* **2**, 8–13 (2016).

20. S. K. Loeb *et al.*, Nanoparticle enhanced interfacial solar photothermal water disinfection demonstrated in 3-D printed flow-through reactors. *Environ. Sci. Technol.* **53**, 7621–7631 (2019).

21. M. Maillard, P. Huang, L. Brus, Silver nanodisk growth by surface plasmon enhanced photoreduction of adsorbed [Ag$^+$]. *Nano Lett.* **3**, 1611–1615 (2003).

22. R. Jin *et al.*, Photoinduced conversion of silver nanospheres to nanoprisms. *Science* **294**, 1901–1903 (2001).

23. L. Zhou *et al.*, Aluminum nanocrystals as a plasmonic photocatalyst for hydrogen dissociation. *Nano Lett.* **16**, 1478–1484 (2016).

24. S. Mukherjee *et al.*, Hot-electron-induced dissociation of H$_2$ on gold nanoparticles supported on SiO$_2$. *J. Am. Chem. Soc.* **136**, 64–67 (2014).

25. S. Mukherjee *et al.*, Hot electrons do the impossible: Plasmon-induced dissociation of H$_2$ on Au. *Nano Lett.* **13**, 240–247 (2013).

26. P. Christopher, H. Xin, S. Linic, Visible-light-enhanced catalytic oxidation reactions on plasmonic silver nanostructures. *Nat. Chem.* **3**, 467–472 (2011).

27. M. W. Knight *et al.*, Embedding plasmonic nanostructure diodes enhances hot electron emission. *Nano Lett.* **13**, 1687–1692 (2013).

28. J. S. DuChene, G. Tagliabue, A. J. Welch, W.-H. Cheng, H. A. Atwater, Hot hole collection and photoelectrochemical CO$_2$ reduction with plasmonic Au/p-GaN photocathodes. *Nano Lett.* **18**, 2545–2550 (2018).

29. K. Li *et al.*, Balancing near-field enhancement, absorption, and scattering for effective antenna–reactor plasmonic photocatalysis. *Nano Lett.* **17**, 3710–3717 (2017).

30. H. Robatjazi *et al.*, Plasmon-induced selective carbon dioxide conversion on earth-abundant aluminum-cuprous oxide antenna-reactor nanoparticles. *Nat. Commun.* **8**, 27 (2017).

31. C. Zhang *et al.*, Al–Pd nanodisk heterodimers as antenna–reactor photocatalysts. *Nano Lett.* **16**, 6677–6682 (2016).

32. R. P. Schwarzenbach *et al.*, The challenge of micropollutants in aquatic systems. *Science* **313**, 1072–1077 (2006).

33. R. L. Johnson, P. G. Tratnyek, R. O. B. Johnson, Persulfate persistence under thermal activation conditions. *Environ. Sci. Technol.* **42**, 9350–9356 (2008).

34. T. Zhang *et al.*, Efficient peroxydisulfate activation process not relying on sulfate radical generation for water pollutant degradation. *Environ. Sci. Technol.* **48**, 5868–5875 (2014).

35. Y. Qian *et al.*, Perfluorooctanoic acid degradation using UV–persulfate process: Modeling of the degradation and chlorate formation. *Environ. Sci. Technol.* **50**, 772–781 (2016).

36. J. Costanza, G. Otaño, J. Callaghan, K. D. Pennell, PCE oxidation by sodium persulfate in the presence of solids. *Environ. Sci. Technol.* **44**, 9445–9450 (2010).

37. Z. Wei, F. A. Villamena, L. K. Weavers, Kinetics and mechanism of ultrasonic activation of persulfate: An in situ EPR spin trapping study. *Environ. Sci. Technol.* **51**, 3410–3417 (2017).

38. G. Fang, J. Gao, D. D. Dionysiou, C. Liu, D. Zhou, Activation of persulfate by quinones: Free radical reactions and implication for the degradation of PCBs. *Environ. Sci. Technol.* **47**, 4605–4611 (2013).

39. C. Kim, J.-Y. Ahn, T. Y. Kim, W. S. Shin, I. Hwang, Activation of persulfate by nanosized zero-valent iron (NZVI): Mechanisms and transformation products of NZVI. *Environ. Sci. Technol.* **52**, 3625–3633 (2018).

40. H. Hori *et al.*, Efficient decomposition of environmentally persistent perfluorocarboxylic acids by use of persulfate as a photochemical oxidant. *Environ. Sci. Technol.* **39**, 2383–2388 (2005).

41. M. Lattuada, T. A. Hatton, Synthesis, properties and applications of Janus nanoparticles. *Nano Today* **6**, 286–308 (2011).

42. B. Nikoobakht, M. A. El-Sayed, Preparation and growth mechanism of gold nanorods (NRs) using seed-mediated growth method. *Chem. Mater.* **15**, 1957–1962 (2003).

43. C. J. Johnson, E. Dujardin, S. A. Davis, C. J. Murphy, S. Mann, Growth and form of gold nanorods prepared by seed-mediated, surfactant-directed synthesis. *J. Mater. Chem.* **12**, 1765–1770 (2002).

44. B. Nikoobakht, M. A. El-Sayed, Evidence for bilayer assembly of cationic surfactants on the surface of gold nanorods. *Langmuir* **17**, 6368–6374 (2001).

45. C. Graf, D. L. Vossen, A. Imhof, A. van Blaaderen, A general method to coat colloidal particles with silica. *Langmuir* **19**, 6693–6700 (2003).

46. I. Pastoriza-Santos, J. Pérez-Juste, L. M. Liz-Marzán, Silica-coating and hydrophobation of CTAB-stabilized gold nanorods. *Chem. Mater.* **18**, 2465–2467 (2006).

47. I. Gorelikov, N. Matsuura, Single-step coating of mesoporous silica on cetyltrimethyl ammonium bromide-capped nanoparticles. *Nano Lett.* **8**, 369–373 (2008).

48. L. M. Liz-Marzán, M. Giersig, P. Mulvaney, Synthesis of nanosized gold–silica core-–shell particles. *Langmuir* **12**, 4329–4335 (1996).

49. Z. Zhang *et al.*, Mesoporous silica-coated gold nanorods as a light-mediated multifunctional theranostic platform for cancer treatment. *Adv. Mater.* **24**, 1418–1423 (2012).

50. R. Ghosh Chaudhuri, S. Paria, Core/shell nanoparticles: Classes, properties, synthesis mechanisms, characterization, and applications. *Chem. Rev.* **112**, 2373–2433 (2012).

51. Y. Kobayashi, M. A. Correa-Duarte, L. M. Liz-Marzán, Sol–gel processing of silica-coated gold nanoparticles. *Langmuir* **17**, 6375–6379 (2001).

52. A. E. Schlather *et al.*, Hot hole photoelectrochemistry on Au@ SiO$_2$@ Au nanoparticles. *J. Phys. Chem. Lett.* **8**, 2060–2067 (2017).

53. A. Subramania, S. L. Devi, Polyaniline nanofibers by surfactant-assisted dilute polymerization for supercapacitor applications. *Polym. Adv. Technol.* **19**, 725–727 (2008).

54. Y. Y. Ahn *et al.*, Activation of peroxymonosulfate by surface-loaded noble metal nanoparticles for oxidative degradation of organic compounds. *Environ. Sci. Technol.* **50**, 10187–10197 (2016).

55. Y. Y. Ahn *et al.*, Surface-loaded metal nanoparticles for peroxymonosulfate activation: Efficiency and mechanism reconnaissance. *Appl. Catal. B* **241**, 561–569 (2019).

56. H. Lee *et al.*, Activation of persulfates by graphitized nanodiamonds for removal of organic compounds. *Environ. Sci. Technol.* **50**, 10134–10142 (2016).

57. T. A. Baker, C. M. Friend, E. Kaxiras, Nature of Cl bonding on the Au(111) surface: Evidence for a mainly covalent interaction. *J. Am. Chem. Soc.* **130**, 3720–3721 (2008).

58. Y. Yang, J. J. Pignatello, J. Ma, W. A. Mitch, Comparison of halide impacts on the efficiency of contaminant degradation by sulfate and hydroxyl radical-based advanced oxidation processes (AOPs). *Environ. Sci. Technol.* **48**, 2344–2351 (2014).

59. W. Zhang *et al.*, Impact of chloride ions on UV/H$_2$O$_2$ and UV/persulfate advanced oxidation processes. *Environ. Sci. Technol.* **52**, 7380–7389 (2018).

60. X. Gu *et al.*, Oxidation of 1,1,1-trichloroethane stimulated by thermally activated persulfate. *Ind. Eng. Chem. Res.* **50**, 11029–11036 (2011).

61. C. Zhu *et al.*, Reductive hexachloroethane degradation by S$_2$O$_8^{\bullet-}$ with thermal activation of persulfate under anaerobic conditions. *Environ. Sci. Technol.* **52**, 8548–8557 (2018).

62. P. Christopher, H. Xin, A. Marimuthu, S. Linic, Singular characteristics and unique chemical bond activation mechanisms of photocatalytic reactions on plasmonic nanostructures. *Nat. Mater.* **11**, 1044–1050 (2012).

63. J. Lee, U. von Gunten, J. H. Kim, Persulfate-based advanced oxidation: Critical assessment of opportunities and roadblocks. *Environ. Sci. Technol.* **54**, 3064–3081 (2020).

64. D. C. Ratchford, Plasmon-induced charge transfer: Challenges and outlook. *ACS Nano* **13**, 13610–13614 (2019).

65. R. Sundararaman, P. Narang, A. S. Jermyn, W. A. Goddard 3rd, H. A. Atwater, Theoretical predictions for hot-carrier generation from surface plasmon decay. *Nat. Commun.* **5**, 5788 (2014).

66. Y. Q. Huang *et al.*, Bisphenol A (BPA) in China: A review of sources, environmental levels, and potential human health impacts. *Environ. Int.* **42**, 91–99 (2012).

67. S. Balgooyen, P. J. Alaimo, C. K. Remucal, M. Ginder-Vogel, Structural transformation of MnO$_2$ during the oxidation of bisphenol A. *Environ. Sci. Technol.* **51**, 6053–6062 (2017).

68. H. Xu, W. J. Cooper, J. Jung, W. Song, Photosensitized degradation of amoxicillin in natural organic matter isolate solutions. *Water Res.* **45**, 632–638 (2011).

69. K. Li *et al.*, Molecular mechanisms of PFOA-induced toxicity in animals and humans: Implications for health risks. *Environ. Int.* **99**, 43–54 (2017).

70. C. Hanske, M. N. Sanz-Ortiz, L. M. Liz-Marzán, Silica-coated plasmonic metal nanoparticles in action. *Adv. Mater.* **30**, e1707003 (2018).

ENGINEERING

Wei et al.

www.manaraa.com